J. Fluid Mech. (1993), *vol.* 248, *pp.* 363–381

Instability waves on the air–sea interface

By G. H. WHELESS AND G. T. CSANADY
Center for Coastal Physical Oceanography, Old Dominion University, Norfolk, VA 23529-0276, USA

(Received 2 December 1991 and in revised form 14 September 1992)

We used a compound matrix method to integrate the Orr–Sommerfeld equation in an investigation of short instability waves ($\lambda < 6$ cm) on the coupled shear flow at the air–sea interface under suddenly imposed wind (a gust model). The method is robust and fast, so that the effects of external variables on growth rate could easily be explored. As expected from past theoretical studies, the growth rate proved sensitive to air and water viscosity, and to the curvature of the air velocity profile very close to the interface. Surface tension had less influence, growth rate increasing somewhat with decreasing surface tension. Maximum growth rate and minimum wave speed nearly coincided for some combinations of fluid properties, but not for others.

The most important new finding is that, contrary to some past order of magnitude estimates made on theoretical grounds, the eigenfunctions at these short wavelengths are confined to a distance of the order of the viscous wave boundary-layer thickness from the interface. Correspondingly, the perturbation vorticity is high, the streamwise surface velocity perturbation in typical cases being five times the orbital velocity of free waves on an undisturbed water surface. The instability waves should therefore be thought of as fundamentally different flow structures from free waves: given their high vorticity, they are akin to incipient turbulent eddies. They may also be expected to break at a much lower steepness than free waves.

1. Introduction

Radar probing of the sea surface has focused renewed attention on the small-scale structures readily visible on a wind-blown water surface. Although apparent to the casual observer, they are hard to quantify, understand or conceptualize physically, given their ephemeral and complex nature. For some time now it has been clear that these small-scale structures act as the 'roughness elements' of the sea surface, in that they interact with the turbulent air flow to extract more momentum from the wind than a smooth surface would (but not much more), and to transfer it to the deeper shear flow of the oceanic mixed layer, possibility via a circuitous route involving longer waves. It is only recently, however, that we have begun to gain significant insight into the physics of the small-scale structures, from innovative laboratory investigations (reviewed by Toba 1985), and theoretical studies of the temporal stability of the combined air–water shear flow (Valenzuela 1976; Kawai 1979; van Gastel, Janssen & Komen 1985).

Patches of short waves appearing on a quiescent lake under a wind gust are known as 'cat's paws'. Similar intermittent roughening of the surface is also evident on a raging sea. The theoretical idealization is suddenly imposed spatially uniform wind, over still water. This can also be fairly well approximated in the laboratory. The rapid appearance of waves is reasonably attributed to the hydrodynamic instability

of the shear flow at the air–water interface. Wuest (1949), and later independently Lock (1954), were the first to treat the interface instability problem in the classical theoretical framework of Rayleigh, Tollmien, Schlichting and others. Supposing parallel viscous shear flow in air and water, they determined approximate stability criteria by analytical means. Both Wuest and Lock wrote down the four boundary conditions at the air–water interface, expressing the continuity of two velocity and two stress components. Compared to the boundary layer over a flat plate, these boundary conditions greatly complicate the problem.

Miles (1957*a*) attempted to simplify the problem by satisfying the inviscid boundary conditions (continuity of normal velocity and stress) rigorously, but making approximate allowances for boundary layers. The work of Miles attracted considerable attention, sparking renewed interest in the use of stability models to examine the wind-wave generation problem. It was not until the advent of microwave radar probing of the sea surface that Valenzuela (1976) returned to the full formulation of the interface instability problem, and showed by numerical integration of the Orr–Sommerfeld equation that the waves with highest growth rates fall into the gravity–capillary range important for scatterometry. Kawai (1979) carried out an extensive investigation of the growth rate of short instability waves as a function of wavenumber, both through the numerical integration of the Orr–Sommerfeld equation, and laboratory observation. His results established beyond doubt that short wind waves arise on a quiescent wind-blown surface on account of the instability of the coupled air–water shear flow, very much as turbulence arises in a boundary layer. Kawai also found that the wave speed of the instability waves is essentially the same as theory predicts for free waves, allowing for advection by the shear flow. As is well known, gravity–capillary waves have minimum wave speed at a wavelength of about 1.7 cm. Kawai's results showed that the maximum growth rate of the instability waves, as a function of wavelength, nearly coincided with minimum wave speed. We found this intriguing, and embarked on an investigation of exactly how fluid properties affect the growth rate of the instability waves.

An analytical investigation of the same problem by van Gastel *et al.* (1985) has led to the conclusion that surface tension is of subordinate importance, so that, by implication, the coincidence of minimum wave speed and maximum growth rate had to be fortuitous. Other results were that the velocity profile in air had a first-order effect on growth rate (as Miles had shown), and so had the viscosity in water and air. Van Gastel *et al.* concluded also that wave growth was mainly due to pressure work, the shear stress perturbation being negligible. The conclusions were reached on the basis of order of magnitude estimates involving fractional powers of a moderately small parameter.

The investigations of Valenzuela, Kawai, and van Gastel *et al.* all focused on the growth rate of the instability waves, and the internal structure of those waves remained unexplored. The two numerical studies extended only to a limited range of parameter space, while the accuracy of the analytical study of van Gastel *et al.* was difficult to assess. A robust and efficient numerical technique held out the promise that these gaps in understanding could be bridged. Such a technique was kindly suggested to us by Chester Grosch, and became the cornerstone of our work.

While this method allowed us to calculate growth rates and eigenfunctions with little difficulty, it imposed some limitations on the mean profile to be treated. In order to have enough resolution between the interface and the critical layer (a very short span), a dense grid had to be used, which then limited the distance to which the

integration could reasonably be carried. This was acceptable, because the perturbations of interest were evanescent beyond a millimetre or two of the interface. However, the mean velocity profiles had to be truncated in such a way that their outer regions were unrealistic. Furthermore, our computational method could not cope with the near-discontinuity in the second derivative of the mean air velocity profile, $U''_a(z)$, characterizing the linear-logarithmic profile used in previously theoretical investigations. We therefore used profiles with a smooth variation of $U''_a(z)$.

The calculations revealed that, as may be expected, the value of $U''_a(z)$ near the interface (and the critical layer: the two are very close for short waves) had a major effect on growth rate. Viscosities of the two media are also important, although their effect is less than that of $U''_a(z)$. Surface tension affects the growth rate only slightly, and the wavelength of the fastest growing wave lessens with a reduction in surface tension, but not as much as the wavelength of minimum wave speed. For the most part these results are in agreement with conclusions of previous studies.

The major new insight we gained came from the calculation of the eigenfunctions: they turned out to be dominated by the 'viscid' solutions of the Orr–Sommerfeld equation. A simple heuristic argument justifying this result runs as follows. As a wavelet at its crest 'compresses' the steep velocity gradient in the air, a large perturbation velocity appears on the air side of the interface. The horizontal velocity being continuous, the same perturbation is transmitted to the water. The inviscid solution in the water, which is very similar to a free wave, has a much smaller surface velocity (for given amplitude) so that a viscid solution is required to satisfy the boundary condition of velocity continuity.

The internal flow structure of the instability waves thus differs dramatically from the structure of free waves. While the surface moves as in a free wave, the motion below amounts to shallow vortices growing rapidly. At even a small finite amplitude, these should form rollers, causing the waves to 'break', in the sense of the surface fluid overtaking the wave. In other words, instability waves may be characterized as incipient turbulent eddies peculiar to a free surface.

2. Model of the shear flow

To repeat a few key points, Kawai (1979) showed that (i) hydrodynamic instability is responsible for the wind-induced ruffling of an initially smooth water surface, and (ii) the ruffles behave as gravity–capillary waves with a wave speed near minimum, and wavenumber of order 3 cm^{-1}. As did Kawai, we assume that linear instability waves on the combined air–water shear flow constitute a valid model of the ruffles. We will explore the effect of external variables on the growth rate and wave speed of the instability waves, and determine their internal flow structure, by numerical integration of the Orr–Sommerfeld equation.

The mean velocity $U(z)$, and its second derivative $U''(z)$, play an important role in the equation. As is verified *a posteriori*, the perturbation flow associated with the instability waves is significant only very close to the interface, so that only the innermost portion of the velocity profiles in air and water matters. On the other hand, high resolution is required in the thin active region of the perturbations, making it impractical to integrate much further from the interface than the outer limit of the active regions. The imposition of an artificial top or floor is known to yield spurious modes in the resulting eigenfunction spectrum (Lakin & Grosch 1982). Therefore we have truncated the velocity distribution in the air by choosing simple

integrable functions for $U_a''(z)$, so as to yield a realistic velocity distribution within the range of significant perturbation amplitude. Outside that range the velocity approaches a constant value which is only about half the typical wind speed a metre or two above the sea surface. The water side is less important in the problem, and a simple exponential velocity distribution is adequate.

2.1. *Air flow model*

The highly idealized 'wind-gust' model underlying the calculations, which also approximates conditions in the laboratory experiments on wave generation, supposes constant shear stress impulsively imposed over a smooth water surface and remaining constant in time and space. The stress is continuous across the interface, and defines friction velocities u_* on the two sides:

$$\tau = \rho_a u_{*a}^2 = \rho_w u_{*w}^2 = \rho_a \nu_a U_a'(0) = \rho_w \nu_w U_w'(0), \tag{1}$$

where subscript a stands for air side, w for water side. On the air side, the velocity distribution rapidly becomes similar to fully developed turbulent flow over a smooth flat plate: in laboratory studies this occurs within approximately 1 s (Larson & Wright 1975). Of importance here are velocities close to the water surface, in the 'inner' or 'wall' region of the turbulent boundary layer. The velocity distribution in this region is linear with height in a viscous sublayer, logarithmic beyond. Kawai (1979) used an interpolation formula due to Miles (1957*b*), patching a linear to a logarithmic function. Where the two meet, $U_a''(z)$ is nearly discontinuous, a feature not only troublesome computationally but also unphysical.

To construct a better model, let conventional non-dimensional variables $U^+ = (U_a - U_0)/u_{*a}$ and $z^+ = u_{*a} z/\nu_a$ describe the inner-law velocity distribution on the air side (U_0 is the water surface velocity). In terms of these variables, but writing $U(z)$ for $U^+(z^+)$ for simplicity, surface conditions on the velocity profile are

$$U(0) = 0, \quad U'(0) = 1. \tag{2}$$

Supposing the velocity gradient to vanish at large z, and the second derivative to be integrable, the following integral constraints on $U''(z)$ emerge:

$$\int_0^\infty U''(z)\,\mathrm{d}z = -1, \quad \int_0^\infty zU''(z)\,\mathrm{d}z = -U_\infty, \tag{3a,b}$$

where U_∞ is the free-stream air velocity. A simple function for a smooth second velocity derivative, with a maximum at the interface and monotonic decay, is one half of a Gaussian distribution:

$$U''(z) = -A\exp(-b^2z^2), \tag{4}$$

with A, b constants. By (3) the constants have to satisfy

$$A/b = 2\pi^{-\frac{1}{2}}, \quad A/b^2 = 2U_\infty, \tag{5}$$

so that $b = \pi^{-\frac{1}{2}}U_\infty^{-1}$, $A = 2\pi^{-\frac{1}{2}}U_\infty^{-1}$. Integration of (4) yields the shear and velocity profiles:

$$U'(z) = \operatorname{erfc}(bz), \quad U(z) = U_\infty(1 - \pi^{\frac{1}{2}}\operatorname{ierfc}[bz]). \tag{6}$$

The only adjustable parameter is U_∞. As illustrated in figure 1, choosing a value near 13 for U_∞ results in a realistic velocity profile to about $z^+ = 30$, acceptable for our purpose.

A reviewer has pointed out that in a steady flow without a pressure gradient the velocity profile curvature vanishes at the wall, in a boundary layer. The same

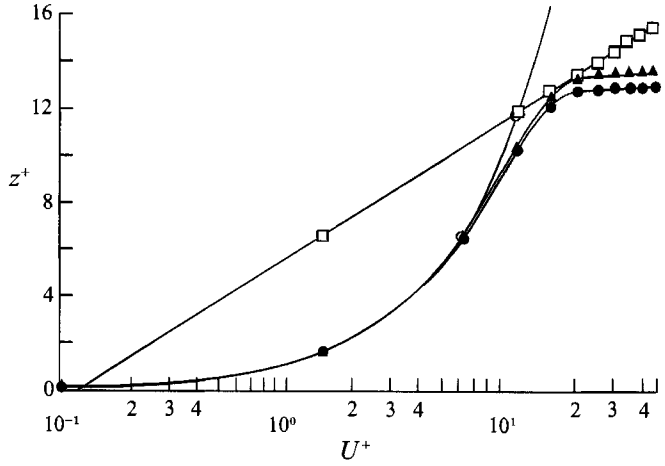

FIGURE 1. Comparison of the two air profiles used in this study (●, ierfc profile according to (6.) ▲, $U''(0) = 0$ according to (7)) with a linear profile (○) and a logarithmic profile (□), showing the region of validity. Plotted on the standard z^+ and U^+ axes.

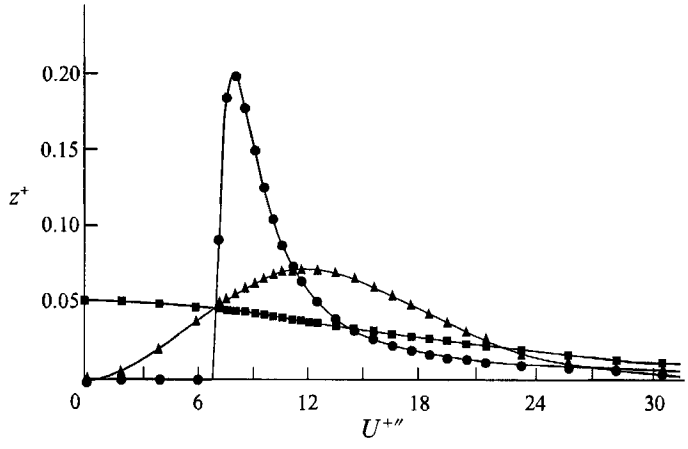

FIGURE 2. Air velocity profile curvature comparison. The difference between the ierfc profile (■), the $U''(0) = 0$ profile (▲) and the standard linear-logarithmic profile (●) is evident in this comparison of the curvature of each.

condition also applies, to a high degree of approximation, over a water surface. The finite $U''(0)$ value in (4) can perhaps be justified in a gust model as due to downwind pressure gradient. It is more satisfactory, however, to investigate a profile that does satisfy the required conditions without invoking such an excuse. In the absence of a pressure gradient the second velocity derivative should vary as z^2 near the surface (Chapman & Kuhn 1986). A straightforward modification of our previous approach is to set

$$U''(z) = -Cz^2 \exp(-b^2 z^2) \tag{7}$$

with $Cb^{-3} = 4\pi^{\frac{1}{2}}$ and $Cb^{-4} = 2U_\infty$ so that $b = 2\pi^{-\frac{1}{2}} U_\infty^{-1}$, $C = 32\pi^{-2} U_\infty^{-3}$.

With a choice of U_∞ close to 13, this formula again yields a realistic velocity distribution to about $z^+ = 30$, again see figure 1.

The second derivatives according to the above two formulae, with constants as in figure 1, are compared with Miles interpolation formula in figure 2. The centre of gravity of the areas under the curves is at U_∞, as (3*b*) shows.

3.3. *Velocity profile on the water side*

On the water side the velocity profile is slower to develop, on account of lower kinematic viscosity. The viscous boundary layer remains thin enough for several seconds for laminar flow to persist. In that layer, a model of parallel laminar flow, due to impulsively applied constant shear stress, yields a good approximation to the observed mean velocity distribution (Kawai 1979). The model profile is of the same functional form as one of the air velocity profiles discussed above:

$$U_{\mathrm{w}}(z) = \frac{u_{*\mathrm{w}}^2 L_{\mathrm{s}}}{\nu_{\mathrm{w}}} \mathrm{ierfc}\,(-z/L_{\mathrm{s}}), \tag{8}$$

where $L_{\mathrm{s}} = 2(\nu_{\mathrm{w}} T)^{\frac{1}{2}}$, the viscous boundary layer depth T s after the application of the surface stress. As implied by the notation, L_{s} serves as a convenient lengthscale, with a typical value of a few millimetres. The value of the surface velocity is then

$$U_0 = u_{*\mathrm{w}}^2 L_{\mathrm{s}} (\pi \nu_{\mathrm{w}})^{-\frac{1}{2}} = (u_{*\mathrm{a}} \pi^{-\frac{1}{2}})\,(\mu_{\mathrm{a}} \mu_{\mathrm{w}}^{-1})\,(u_{*\mathrm{a}} L_{\mathrm{s}} \nu_{\mathrm{a}}^{-1}), \tag{9}$$

where $\mu = \rho\nu$ is dynamic viscosity. U_0 is again a multiple of the velocity scale on the air side, $u_{*\mathrm{a}}$. The velocities and velocity gradients on the water side of the interface are, however, much smaller than on the air side, and affect the integration little. Of the water-side profile parameters only the surface velocity and depth of the boundary layer are important. In the computations we have used a simplified velocity distribution, namely

$$U_{\mathrm{w}}(z) = U_0 \exp\,(2zL_{\mathrm{s}}^{-1}), \tag{10}$$

which coincides with the profile given by (9) over the range of significant velocities.

The 'natural' lengthscales on the two sides of the interface, L_{s} and $\nu_{\mathrm{a}} u_{*\mathrm{a}}^{-1}$ differ, the latter being inconveniently small. We have used L_{s} as the common lengthscale in our calculations, translating the air-side profile appropriately. Although the obvious choice for a velocity scale is $u_{*\mathrm{a}}$, U_∞ is more convenient because it yields non-dimensional velocities of order one.

3. The eigenvalue problem

Let all lengths now be expressed as multiples of L_{s}, all velocities as multiples of U_∞. Reynolds numbers in air and water are then $R_{\mathrm{a}} = U_\infty L_{\mathrm{s}}/\nu_{\mathrm{a}}$, $R_{\mathrm{w}} = U_\infty L_{\mathrm{s}}/\nu_{\mathrm{w}}$. A disturbance streamfunction is introduced:

$$\Psi(x, z; t) = \phi(z) \exp\,[\mathrm{i}k(x - ct)], \tag{11}$$

where $\phi(z)$ is the amplitude distribution. The scaled Navier–Stokes equations for an incompressible fluid may be linearized and the pressure eliminated to yield the Orr–Sommerfeld equation (OSE) for the amplitude distribution. In the air, this is

$$(U_{\mathrm{a}} - c)\,(\phi_{\mathrm{a}}'' - \phi_{\mathrm{a}} k^2) - U_{\mathrm{a}}''\phi_{\mathrm{a}} = (\mathrm{i}kR_{\mathrm{a}})^{-1}\phi_{\mathrm{a}}^{\mathrm{iv}} - 2k^2\phi_{\mathrm{a}}'' + k^4\phi_{\mathrm{a}}, \tag{12}$$

and in the water

$$(U_{\mathrm{w}} - c)\,(\phi_{\mathrm{w}}'' - \phi_{\mathrm{w}} k^2) - U_{\mathrm{w}}''\phi_{\mathrm{w}} = (\mathrm{i}kR_{\mathrm{w}})^{-1}\phi_{\mathrm{w}}^{\mathrm{iv}} - 2k^2\phi_{\mathrm{w}}'' + k^4\phi_{\mathrm{w}}. \tag{13}$$

With a mean velocity distribution prescribed, these equations may be integrated in principle, for a chosen complex value of c. The approach used here is to perform a 'top-down' numerical integration in the air, and a 'bottom-up' integration in the

water. The resulting solutions must then be made to satisfy the boundary conditions at the interface by an appropriate choice of the eigenvalue, c.

At $z = \pm\infty$, both disturbance velocity components must vanish, which in terms of the disturbance amplitude, $\phi(z)$, means that

$$\phi(z) = \phi'(z) = 0, \quad z = \pm\infty. \tag{14}$$

The boundary conditions at the air–sea interface are much more complicated than over a solid surface. Both components of the velocity and shear stress must be continuous. The normal pressure is discontinuous between the water and air, the difference being balanced by the surface tension force over a curved interface. The linearized free surface boundary conditions, neglecting surface tension gradients or film effects, have been written down by Wuest (1949) and later workers. They are

$$\phi_a = \phi_w, \tag{15}$$

$$\frac{U'_a}{c-U_0}\phi_a + \phi'_a = \frac{U'_w}{c-U_0}\phi_w + \phi'_w, \tag{16}$$

$$\frac{\mu_a}{\mu_w}\left[\left(\frac{U''_a}{c-U_0}+k^2\right)\phi_a+\phi''_a\right] = \left(\frac{U''_w}{c-U_o}+k^2\right)\phi_w+\phi''_w, \tag{17}$$

$$\frac{\rho_a}{\rho_w}\left[\left(U'_a-\frac{kC_0^2}{c-U_0}\right)\phi_a+(c-U_0+3ikR_a^{-1})\,\phi'_a+\frac{\phi'''_a}{ikR_a}\right]$$

$$= \left(U'_w-\frac{kC_0^2}{c-U_0}\right)\phi_w+(c-U_0+3ikR_w^{-1})\,\phi'_w+\frac{\phi'''_w}{ikR_w}, \tag{18}$$

where C_0^2 is the wave speed of free-surface waves of wavenumber k. Satisfying these four conditions simultaneously is a major difficulty in finding the eigenvalues.

4. Numerical procedure

The chief difficulty in numerical solution of the OSE is that the viscid portion of the total solution varies on a much shorter scale than does the inviscid portion, rendering the OSE very 'stiff' near the interface. To overcome this difficulty, we used the compound matrix method, a numerical technique which combines the inviscid and viscid solutions through the use of a Ricatti transformation. A complete explanation of the method and its application in obtaining the eigenfunctions of the instability waves may be found in the Appendix.

The numerical computations were performed in the following manner. Initial conditions for the transformed OSE terms, $y(z)$, at large $\pm z$ were calculated from (A 15) and (A 17) using a trial scaled complex eigenvalue c, a fixed scaled wavenumber k, and the appropriate Reynolds number. The integration of these $y(z)$ terms from $z = \pm\infty$ to $z = 0$, employed a fourth-order Runge–Kutta scheme. The values of $y_w(0)$ and $y_a(0)$ obtained from the integrations were then used in (A 22) to calculate the value of the determinant. The bottom-up and top-down integration procedure was repeated twice more with slightly different trial eigenvalues, generating three error values. Muller's method (Gerald & Wheatly 1984, p. 35, an iterative method which finds the complex root of a quadratic fitted to the three pairs of trial eigenvalue-error points) was used to adjust the eigenvalue until the relative error was reduced to an accuracy of at least 10^{-8}. The eigenvalue, a scaled complex wave speed, yielded a scaled disturbance growth rate, kc_i and a frequency, $\omega = kc_r$, at a single wavenumber.

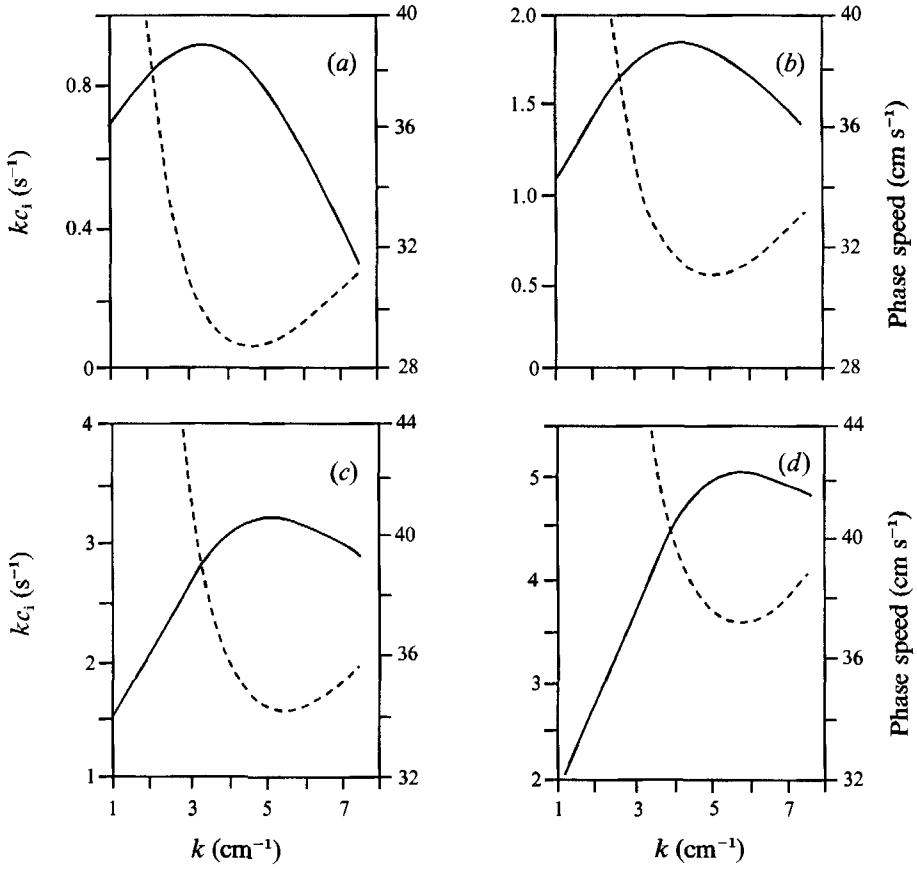

FIGURE 3. Phase speed (c_r) (-----) and growth rate (kc_i) (——) plotted against wavenumber for different shear flow cases. Water-side boundary-layer development time (T) is held constant at 5.0 s for all cases. In all cases shown $L_s = 0.447$ cm. (*a*) $u_{*a} = 15.0$ cm s^{-1}, (*b*) $u_{*a} = 18.0$ cm s^{-1}, (*c*) $u_{*a} = 21.0$ cm s^{-1}, (*d*) $u_{*a} = 24.0$ cm s^{-1}. These plots are similar to Kawai's (1979) and show an apparent, yet fortuitous, connection between minimum c_r and maximum kc_i.

u_{*a} (cm s^{-1})	T (s)	u_0 (cm s^{-1})	U_∞ (cm s^{-1})	L_s	R_a	R_w
15.0	5.0	6.8	197.7	0.447	589	8845
18.0	5.0	9.8	238.9	0.447	712	10688
21.0	5.0	13.4	280.7	0.447	836	12554
24.0	5.0	16.5	345.0	0.447	1023	15235
15.0	10.0	9.63	200	0.632	845	12688
15.0	12.0	10.55	201	0.692	930	13963
15.0	15.0	11.8	202	0.775	1047	15707

TABLE 1. Flow parameters

The eigenvalues for a specific velocity profile were found over a range of wavenumbers, resulting in curves of phase speed and growth rate versus wavenumber, illustrated in figure 3. Similar curves were found for velocity profiles based on different values of u_{*a} (see table 1), as well as for different surface tension and viscosity values. These curves allowed an analysis of the effects of variable flow

parameters, surface tension and viscosity on the growth rate and phase speed of the instability waves.

All calculations were done in complex double-precision fortran on a SUN 4/100 workstation. The domain of the problem was divided into 4000 equally spaced grid points. Convergence to an eigenvalue occurred within four or five iterations, with each iteration taking about 35 s. More iterations were required if the initial trial eigenvalue was far from the actual eigenvalue. Occasionally, stable modes were found.

5. Results: effects of external variables

Our original objective was to explore the effect of external variables on wavelet speed and growth rate, notably the question of whether the coincidence of minimum wave speed and maximum growth rate holds for fluids with a surface tension different from that of pure water. After the choices made for our velocity profiles, fluid properties plus u_{*a} and L_s (a function of the development time T) remained as independent external variables. We varied one of these variables at a time, holding the others constant, at the standard values of $\sigma = 75.0$, $\rho_a = 0.0012$, $\rho_w = 1.0$, $\nu_a = 0.15$, $\nu_w = 0.01$, $L_s = 0.447$ ($T = 5.0$), $u_{*a} = 15.0$, all in c.g.s. units. We also used the half-Gaussian velocity profile of (6) as our standard.

First, we look at the influence of u_{*a}. With L_s fixed, U'' varies as u_*^3, U and Reynolds number vary as u_*. Figure 3 shows calculated wave speed and growth rate against wavenumber, at four different values of u_*. Maximum growth rates increase somewhat faster than u_*^3, and shift to higher wavenumber. At fixed k, however, they grow accurately with u_*^3, hence with U''. The minimum wave speed, and the wavenumber at which it occurs, both increase slowly with u_*. The increase in the value of the wave speed tracks the surface velocity. The change in the wavenumber at which it occurs is a first indication that the instability waves behave differently from free-surface waves.

As in Kawai's results, minimum phase speed and maximum growth rate nearly coincide at all four u_* values in figure 3. The correlation does not survive drastic change in surface tension, however. Figure 4 shows the effect of reducing surface tension to 45 dyn cm^{-1}; the wavenumber of minimum wave speed changes more than the wavenumber of maximum growth rate. There is also a small rise in growth rate with reducing surface tension: this is reasonably attributed to a decrease in the work required to perturb a film-free surface.

Varying air viscosity, at fixed u_* and L_s, increases U'' as ν_a^{-2}. Peak growth rate increases in the same proportion, see figure 5, without significant change of wave speed or of most unstable wavenumber. When we changed ν_a and u_*, but so as to maintain u_a^3/ν_a^2 (hence U'') constant, the maximum growth rate changed by less than 1 %.

Varying water viscosity changes the water-side boundary-layer thickness L_s as $(\nu_w T)^{\frac{1}{2}}$. At fixed development time T the effect on wave speed is minor, tracking the change in surface velocity U_0, see figure 6. The growth rate is more sensitive to ν_w.

The same sensitivity shows up in the variation of the growth rate with development time, or at fixed ν_w, with L_s, figure 7. The three curves shown were calculated with $T = 5$, 8, and 10 s. That water viscosity and development time influence growth rate similarly points to water-side boundary-layer depth as the governing variable. We verified that if L_s is held constant while water viscosity and development time change in opposite directions, growth rate remains unchanged. The strong dependence of

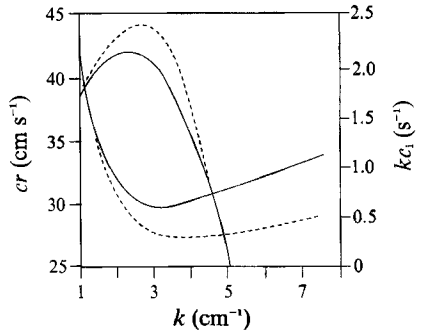

FIGURE 4. Phase speed (c_r) and growth rate (kc_i) plotted against wavenumber for different values of surface tension. Surface tension, σ^*, values are 45.0 (dashed) and 75.0 (solid) dynes cm^{-1}. Shear flow parameters are $u_{*a} = 15.0$ cm s^{-1} and $T = 10.0$ s. Minimum phase speed moves to higher wavenumber as surface tension is decreased. Maximum growth rate moves to higher wavenumber as surface tension is decreased, but far less than the minimum phase speed.

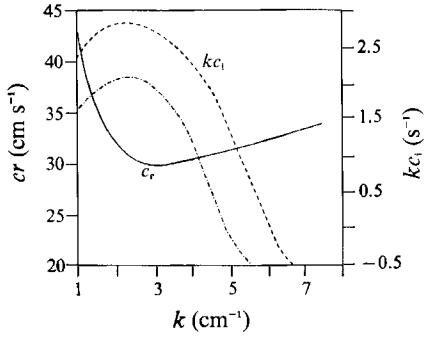

FIGURE 5. Phase speed and growth rate plotted against wavenumber for different values of kinematic viscosity of air, ν_a. Shear flow parameters are as in figure 4. Values of ν_a are 0.12 (dashed) and 0.15 (dash dot) cm^2 s^{-1}. Note that phase speed remains unchanged. Growth rates increase substantially with decreasing ν_a yet maximum growth rate wavenumber does not.

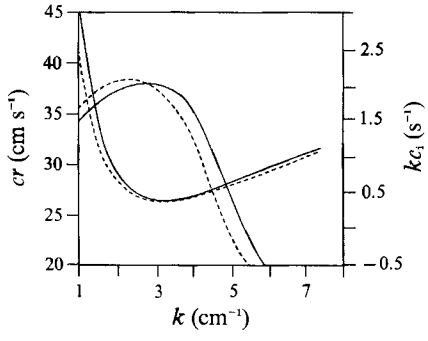

FIGURE 6. Phase speed and growth rate plotted against dimensional wavenumber for different values of viscosity of water, ν_w. Values of ν_w are 0.009 (solid) and 0.10 (dashed) cm^2 s^{-1}. Shear flow parameters are as in figure 4. Note the small effect that variable water viscosity has on the instability wave characteristics.

growth rate on water-side development time is reminiscent of one-sided (flat plate) boundary-layer behaviour, see Schlichting (1979, p. 471). Such a property certainly distinguishes instability waves from free-surface waves. Although both Valenzuela (1976) and van Gastel *et al.* (1985) emphasize the important influence of the water

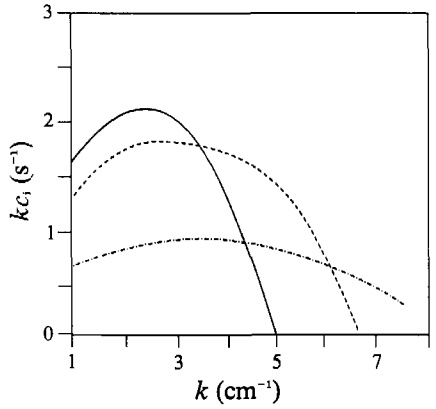

FIGURE 7. Growth rate against dimensional wavenumber for varying boundary-layer thicknesses. Boundary-layer depth is changed by varying boundary layer development time T; u_{*a} is held constant at 15.0 cm s^{-1}. Note how the growth rates increase and the wavelength of the most unstable wave increases as the boundary-layer thickness increases. Development time T: 5.0 s (dash dot); 8.0 s (dashed); 10.0 s (solid).

side on growth rate, the finding that boundary-layer thickness is responsible appears to be new. Figure 7 also shows that the most unstable wavenumber decreases as boundary-layer thickness increases, according to $k_m^{-1} = \text{Constant} \times L_s$, the constant being approximately 1.35. This relationship further ties the instability waves to the water-side boundary layer.

6. Structure of the eigenfunctions

With our method we were able to calculate the eigenfunctions specifying the structure of the instability waves. Real and imaginary parts of the eigenfunction amplitudes, plotted in figure 8 against distance from the interface, reveal that the perturbations are confined to thin layers on the air and the water sides, of a thickness of about 0.1 L_s, or typically 0.2–0.3 mm ($z^+ = 3$ or so). Plotting the corresponding streamfunctions over an entire wavelength (figure 9) makes the interface trapping clearer, and also illustrates the highly vortical nature of the velocity distribution in the instability waves. The surface velocity is typically 5 times higher than in a free wave of the same amplitude.

We have also determined the energy supply from the mean flow to the perturbations, from the standard formula for non-dimensional perturbation stress (Drazin & Reid 1981, p. 221):

$$S(z) = \overline{u'v'} = \phi_r \frac{d\phi_i}{dz} - \phi_i \frac{d\phi_r}{dz}, \tag{19}$$

where ϕ_r and ϕ_i are real and imaginary parts of the perturbation streamfunction. The perturbation stress distribution is also confined to thin interface layers. The energy transfer to the perturbations, $S\,dU/dz$, peaks on the air side of the interface, where the velocity potential is large.

Because of the prominent role of the second velocity derivative in the instability problem, it is important to find out if the change of the $U_a''(z)$ distribution from the Gaussian ansatz to the formula with $U''(0) = 0$, shown in figure 2, makes a major

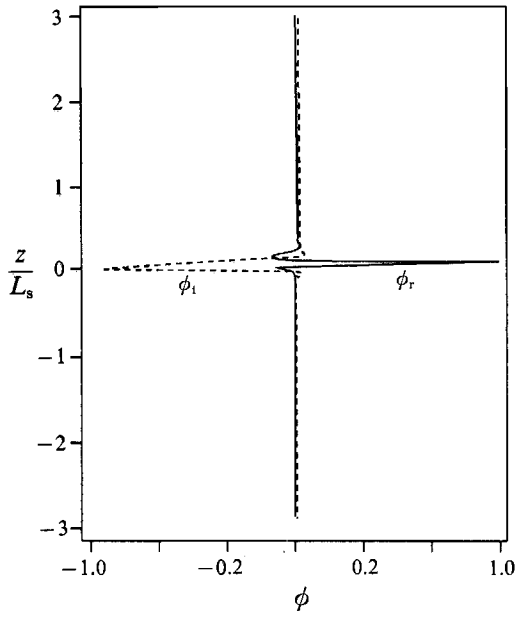

FIGURE 8. Real and imaginary portions of the eigenfunctions in air and water at a wavenumber very close to that of maximum growth rate. Horizontal axis is scaled amplitude, vertical axis is scaled distance above or below the interface. Shear flow parameters are those of figure 4. Note that the disturbance is effectively confined to within $z/L_s < 0.10$ from the interface, or approximately 0.045 cm.

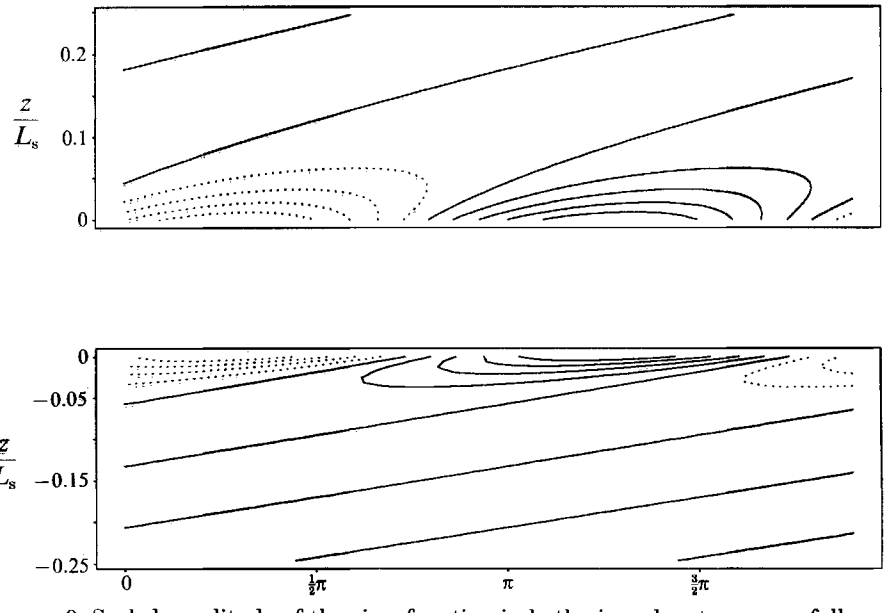

FIGURE 9. Scaled amplitude of the eigenfunction in both air and water over a full wavelength at a wavenumber near that of maximum growth rate. Velocity profile is that with maximum curvature at the interface (ierfc) with parameters as in figure 4. Maximum contour value is that closest to the interface. Contour interval is 0.2 and negative values are dashed. Note the close proximity to the interface of the disturbance.

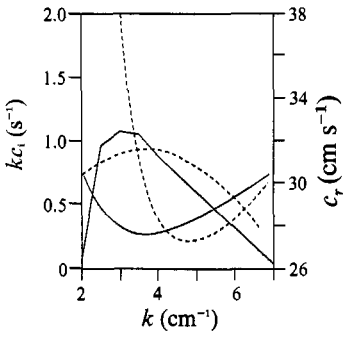

FIGURE 10. Wave speed and growth rate against wavenumber for the air velocity profile with zero curvature at the interface according to (7) (solid) and the ierfc profile with maximum curvature at the interface according to (6) (dashed). In both cases, $T = 5.0$ s and $u_{*a} = 15.0$ cm s^{-1}.

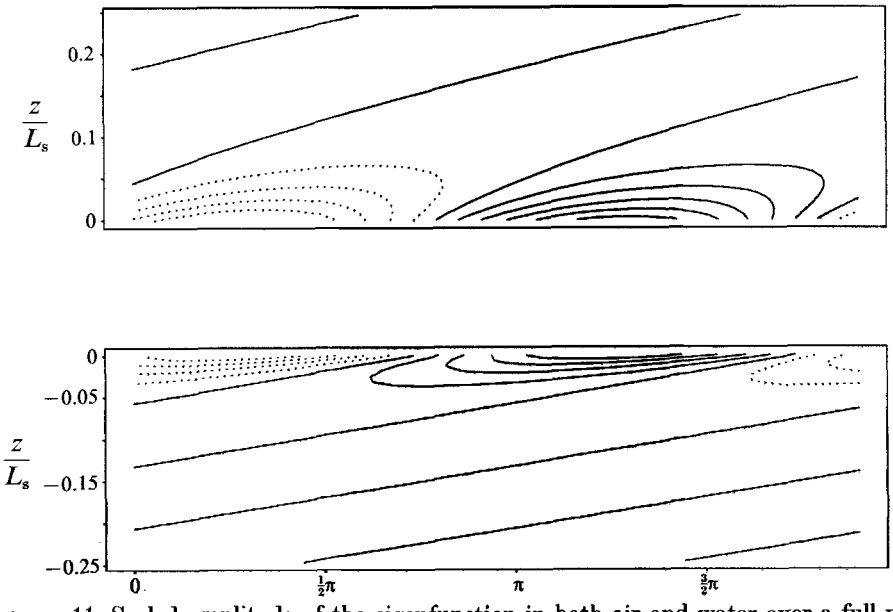

FIGURE 11. Scaled amplitude of the eigenfunction in both air and water over a full wavelength using the air velocity profile of (7) with zero profile curvature at the interface. Wavenumber is near that of maximum growth rate with parameters as in figure 4. Maximum contour value is that closest to the interface. Contour interval is 0.2 and negative values are dashed. Note the close similarity with figure 9.

difference in the calculated results. Figure 10 shows the wave speed and growth rate curves versus wavenumber for the two profiles side by side. There are clearly significant differences, mainly in growth rate but no qualitative change. Somewhat surprisingly, the profile with zero curvature at the origin produces higher maximum growth rate in about the ratio of maximum U''. The perturbation streamlines for the same profile (figure 11) are very similar to the ones shown for the standard case (figure 9), to the point that it takes careful scrutiny to find the differences.

Our calculated growth rates are about twice as high as Kawai's, who used the Miles formula, with a maximum $U_a''(z)$ value three or four times as high as ours, but with vanishing U'' near the interface, see figure 2. The exact reason for the different results is unknown, although velocity profile differences are suspected. We note, however,

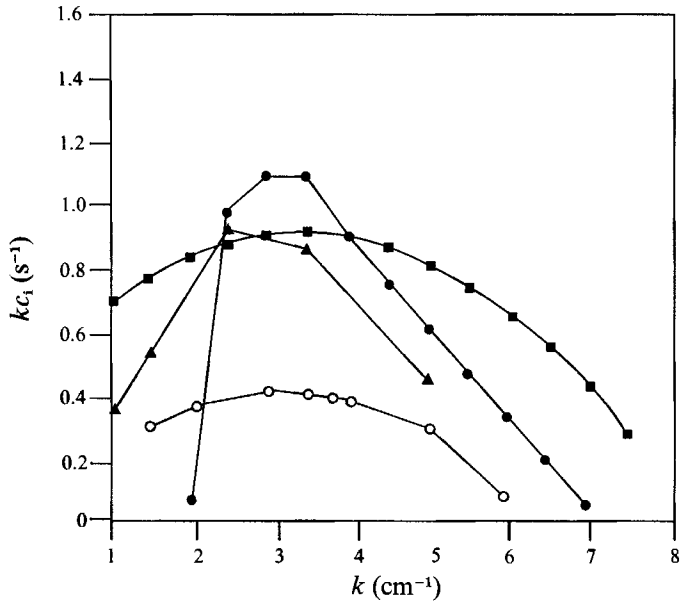

FIGURE 12. Comparison of growth rates for three calculated cases and one observed case using the parameters of figure 4 (except for Kawai's case, where $u_{*a} = 17.0$ cm s^{-1}). ■, ierfc; ●, $U''(0) = 0$; ○, Kawai 1979; ▲, Larson & Wright (1975).

that although Kawai estimated growth rates observed in the laboratory to be similar to what his calculations predicted, Larson & Wright's observed growth rates were higher, close to our results, see figure 12. Kawai determined the wave energy (integrated spectrum) at different development times, and deduced a growth rate from that. This is not quite the same thing as the growth rate of an instability wave of given wavenumber. Larson & Wright used a microwave antenna, and were able to determine the growth rate of a narrow spectral band, which should approximate individual wavelet growth closely.

7. Conclusions

Summing up our past investigations, as well as our results, we catalogue here the properties of instability waves spontaneously appearing under wind on an initially smooth water surface. These 'ruffles' or 'wavelets' travel at a speed close to the speed of a free wave of the same wavenumber. Their growth rate increases rapidly with wind stress (as u_*^3) and peaks at a wavenumber equal to about $0.75L_s$, where L_s is the thickness of the boundary layer developing on the water side of the interface. The air side of the interface affects the growth rate mainly through the second derivative of the velocity $U''(z)$, although the details (e.g. where U'' peaks) are less important, as long as the fairly high values of U'' occur near the interface. The flow structure within the instability waves differs dramatically from free waves, in that most of the forward motion at a crest takes place within a thin layer, a tenth or so of the wave lengthscale k^{-1}. The vorticity in this layer is high, so that the ruffles, while appearing to be wavelets, are also incipient eddies which may be expected to roll up and to form breakers at very modest steepness.

The intriguing coincidence of minimum wave speed and maximum growth rate, which had started us on this investigation, turned out to be fortuitous. It is due to

the circumstance that the water-side boundary layer a few seconds after the start of the wind happens to have a thickness near $0.75k_m^{-1}$, where k_m is the wavenumber of minimum wave speed of free gravity–capillary waves on a water surface.

We wish to thank Dr Chet Grosch for introducing us to the compound matrix method and for the many insightful conversations about this study. This work was supported by the Office of Naval Research under Contract No. N00014-88-K-0101. The first author gratefully acknowledges support from the University Corporation for Atmospheric Research under their Post-doctoral Program in Ocean Modeling. UCAR is supported by the National Science Foundation. Additional resources were provided by the Center for Coastal Physical Oceanography, Old Dominion University.

Appendix

A.1. *The compound matrix method*

This numerical method is an efficient technique which eliminates the problem of runaway growth encountered when the notoriously 'stiff' OSE is integrated by standard shooting methods. The notation used in the description of the method below is taken from Ng & Reid (1979).

The total solution of the OSE, $\phi_T(z)$, where z is positive upwards, is chosen to consist of two linearly independent solutions, an inviscid one $\phi_1(z)$ and a viscid one $\phi_2(z)$. Asymptotically as $z \to \pm\infty$ these solutions are

$$\phi_1(z) = \exp(\pm\alpha z), \quad \phi_2(z) = \exp(\pm\beta z), \tag{A 1}$$

where the + sign applies to the water, the − sign to the air. The choice of sign ensures that the solutions die out in the far field, in accordance with the boundary condition at $z = \pm\infty$. The factors α and β are written down below and are specific for the velocity profile used.

The chief difficulty in numerical solution of the OSE is that as $\beta \gg \alpha$, the viscid solution varies on a much shorter scale than does the inviscid one, rendering the OSE very 'stiff' near the interface. To overcome this difficulty, let $\hat{\boldsymbol{\phi}} = [\phi, \phi', \phi'', \phi''']^T$, where T is the matrix transpose notation. The OSE can then be written as

$$\hat{\boldsymbol{\phi}}' = \boldsymbol{C}(z)\hat{\boldsymbol{\phi}}, \tag{A 2}$$

where

$$\boldsymbol{C}(z) = \begin{bmatrix} 0 & 1 & 0 & 0 \\ 0 & 0 & 1 & 0 \\ 0 & 0 & 0 & 1 \\ C_4 & C_3 & C_2 & C_1 \end{bmatrix}. \tag{A 3}$$

The coefficients $C(z)$ are

$$\begin{aligned} C_1 &= 0, \quad C_2 = 2k^2 + \mathrm{i}kR(U-c), \\ C_3 &= 0, \quad C_4 = -[k^4 + \mathrm{i}kR[k^2(U-c) + U'']], \end{aligned} \tag{A 4}$$

and U and U'' are specified by the shear flow velocity profile. In this manner, the OSE has been rewritten as a system of first-order equations.

The total solution and its derivatives may then be expressed as

$$\phi = A_1\phi_1 + A_2\phi_2, \quad \phi' = A_1\phi_1' + A_2\phi_2', \quad \phi'' = A_1\phi_1'' + A_2\phi_2'', \quad \phi''' = A_1\phi_1''' + A_2\phi_2''', \tag{A 5}$$

where A_1 and A_2 are constants to be determined in such a way as to satisfy the

boundary conditions at the interface. From the two independent solutions, a 4×2 solution matrix is constructed,

$$\boldsymbol{\Phi}(z) = \begin{bmatrix} \phi_1 & \phi_2 \\ \phi_1' & \phi_2' \\ \phi_1'' & \phi_2'' \\ \phi_1''' & \phi_2''' \end{bmatrix} \tag{A 6}$$

Next, a new vector is defined, $\boldsymbol{y} = [y_1 + \ldots + y_6]$, using the 2×2 minors of (A 6),

$$\left.\begin{aligned} y_1 &= \phi_1\phi_2' - \phi_1'\phi_2, & y_4 &= \phi_1'\phi_2'' - \phi_1''\phi_2', \\ y_2 &= \phi_1\phi_2'' - \phi_1''\phi_2, & y_5 &= \phi_1'\phi_2''' - \phi_1'''\phi_2', \\ y_3 &= \phi_1\phi_2''' - \phi_1'''\phi_2, & y_6 &= \phi_1''\phi_2''' - \phi_1'''\phi_2''. \end{aligned}\right\} \tag{A 7}$$

The definition of these y compounds as products of the viscid and inviscid solutions 'mixes' the two, suppressing the rapid variation of the viscid solution and eliminating the 'stiffness' of the equations, allowing them to be integrated using a standard shooting method.

If the $\boldsymbol{y}$ vector is differentiated and the OSE is used to eliminate any ϕ^{iv} terms, the resulting derivatives are linear (Davey 1979). The derivative vector $\boldsymbol{y}'$ has these components:

$$\left.\begin{aligned} y_1' &= y_2, & y_4' &= y_5, \\ y_2' &= y_3 + y_4, & y_5' &= -C_4 y_1 + C_2 y_4 + C_1 y_5 + y_6, \\ y_3' &= C_3 y_1 + C_2 y_2 + C_1 y_3 + y_5, & y_6' &= -C_4 y_2 - C_3 y_4 + C_1 y_6, \end{aligned}\right\} \tag{A 8}$$

In matrix notation, this result is

$$\boldsymbol{y}' = \boldsymbol{B}(z)\,\boldsymbol{y} \tag{A 9}$$

where

$$\boldsymbol{B}(z) = \begin{bmatrix} 0 & 1 & 0 & 0 & 0 & 0 \\ 0 & 0 & 1 & 1 & 0 & 0 \\ C_3 & C_2 & C_1 & 0 & 1 & 0 \\ 0 & 0 & 0 & 0 & 1 & 0 \\ -C_4 & 0 & 0 & C_2 & C_1 & 1 \\ 0 & -C_4 & 0 & -C_3 & 0 & C_1 \end{bmatrix} \tag{A 10}$$

The C_n are as defined in (A 4).

It is clear that (A 9) is a system of linear differential equations with variable coefficients equivalent to (A 2).

A.2. *Initial conditions*

We wish to integrate the OSE in each medium from the far field towards the interface. The amplitude of the disturbance in the air, $\phi_{\mathrm{a}}(z)$, and its derivatives are, asymptotically

$$\begin{aligned} \phi_{1\mathrm{a}}(z) &= [1, -\alpha_{\mathrm{a}}, \alpha_{\mathrm{a}}^2, -\alpha_{\mathrm{a}}^3]^{\mathrm{T}} \exp[(-\alpha_{\mathrm{a}})z], \\ \phi_{2\mathrm{a}}(z) &= [1, -\beta_{\mathrm{a}}, \beta_{\mathrm{a}}^2, -\beta_{\mathrm{a}}^3]^{\mathrm{T}} \exp[(-\beta_{\mathrm{a}})z], \end{aligned} \tag{A 11}$$

The air velocity profile characteristics at a large enough $z = z_{\mathrm{a}}$ are

$$U_{\mathrm{a}}(z_{\mathrm{a}}) = 1, \quad U_{\mathrm{a}}''(z_{\mathrm{a}}) = 0. \tag{A 12}$$

Substituting these profile characteristics into the OSE, the roots of the resulting algebraic expression are found to be

$$\alpha_{\mathrm{a}} = k, \quad \beta_{\mathrm{a}} = [k^2 + \mathrm{i}kR_{\mathrm{a}}(1-c)]^{\frac{1}{2}}. \tag{A 13}$$

The initial conditions for the top-down integration are the y_a terms at $z = z_a$:

$$\left.\begin{aligned}
y_{1a} &= \phi_{1a}\phi'_{2a} - \phi'_{1a}\phi_{2a} = (\alpha_a - \beta_a)\exp[(\alpha_a+\beta_a)z_a],\\
y_{2a} &= \phi_{1a}\phi''_{2a} - \phi''_{1a}\phi_{2a} = (\beta_a^2 - \alpha_a^2)\exp[(\alpha_a+\beta_a)z_a],\\
y_{3a} &= \phi_{1a}\phi'''_{2a} - \phi'''_{1a}\phi_{2a} = (\alpha_a^3 - \beta_a^3)\exp[(\alpha_a+\beta_a)z_a],\\
y_{4a} &= \phi'_{1a}\phi''_{2a} - \phi''_{1a}\phi'_{2a} = \alpha_a\beta_a(\alpha_a - \beta_a)\exp[(\alpha_a+\beta_a)z_a],\\
y_{5a} &= \phi'_{1a}\phi'''_{2a} - \phi'''_a\phi'_{2a} = \alpha_a\beta_a(\beta_a^2 - \alpha_a^2)\exp[(\alpha_a+\beta_a)z_a],\\
y_{6a} &= \phi''_{1a}\phi'''_{2a} - \phi'''_{1a}\phi''_{2a} = (\alpha_a^2\beta_a^2)((\alpha_a - \beta_a)\exp[(\alpha_a+\beta_a)z_a],
\end{aligned}\right\} \tag{A 14}$$

Discarding the common $\{(\alpha_a - \beta_a)\exp[(\alpha_a+\beta_a)z_a]\}$ factor, the system of initial conditions is written in matrix format as

$$y_a(z_a) = [1, -(\alpha_a+\beta_a),\ \alpha_a^2+\alpha_a\beta_a+\beta_a^2,\ \alpha_a\beta_a,\ -\alpha_a\beta_a(\alpha_a+\beta_a),\ \alpha_a^2\beta_a^2]^{\mathrm{T}} \tag{A 15}$$

In like manner, the initial conditions for the bottom-up water integration are found to correspond to (A 14) but with the subscript a replaced by w and $\alpha^i - \beta^i$ replaced by $\beta^i - \alpha^i$ in the expressions for y_{1w}, y_{3w}, y_{4w} and y_{6w}.

where
$$\alpha_w = k, \quad \beta_w = [k^2 - i\omega R_w]^{\frac{1}{2}}. \tag{A 16}$$

After removal of the common factor $\{(\beta_w - \alpha_w)\exp[(\alpha_w+\beta_w)z_w]\}$, this system of initial conditions is written as

$$y_w(z_w) = [1, \alpha_w+\beta_w,\ \alpha_w^2+\alpha_w\beta_w+\beta_w^2,\ \alpha_w\beta_w,\ \alpha_w\beta_w(\alpha_w+\beta_\omega),\ \alpha_w^2\beta_w^2]^{\mathrm{T}}. \tag{A 17}$$

Starting from a moderately large distance above and below the interface, (A 9) is integrated to the surface using the appropriate initial conditions, (A 15) or (A 17), and a trial complex eigenvalue $c = c_r + ic_i$, to begin the procedure. The actual eigenvalue is found by satisfying the four interfacial boundary conditions, a procedure described below.

A.3. *Eigenvalue relation*

An eigenvalue relation for the short-wave generation problem is sought subject to the initial conditions at z_a, (A 15), and at z_w, (A 17), and the interfacial boundary conditions described in the body of this article. A difficulty arises from the fact that the interfacial boundary conditions are written in terms of a four-dimensional vector $\hat{\boldsymbol{\phi}}$, while the solutions obtained from the integration are written in terms of the six-dimensional vector $\boldsymbol{y}$. Upon initial inspection, the problem appears almost impossibly complicated. It is certainly different from that of the boundary layer over a flat plate, where the wall boundary condition is simply $\phi(0) = \phi'(0)$ and the eigenvalue relation in terms of the $\boldsymbol{y}$ compounds is $y_1 = 0$.

As written down in (A 6), the total solutions on the two sides of the interface are linear combinations of the viscid and inviscid solution:

$$\phi_a = A_1\phi_{1a} + A_2\phi_{2a}, \quad \phi_w = A_3\phi_{1w} + A_4\phi_{2w}. \tag{A 18}$$

These forms are substituted into the interface boundary conditions, which may then be written as

$$[\boldsymbol{D}_a - \boldsymbol{D}_w] = 0, \tag{A 19}$$

where
$$\boldsymbol{D}_a = \begin{bmatrix} \phi_{1a} & \phi_{2a} \\ E_a\phi_{1a} + \phi'_{1a} & E_a\phi_{2a} + \phi'_{2a} \\ m[F_a\phi_{1a} + \phi''_{1a}\} & m[F_a\phi_{2a} + \phi''_{2a}] \\ r[H_a\phi_{1a} + I_a\phi'_{1a} + J_a\phi'''_{1a}] & r[H_a\phi_{2a} + I_a\phi'_{2a} + J_a\phi'''_{2a}] \end{bmatrix} \tag{A 20}$$

and a similar expression for $\boldsymbol{D}_{\mathrm{w}}$ but with the subscripts a replaced by w, and without the factors m and r multiplying the third and fourth rows. The variables E, F, H, I and J are written as

$$\left.\begin{gathered} E=\frac{U'(0)}{c-U_0}, \quad F=\frac{U''(0)}{c-U_0}+k^2, \quad H=U'(0)-\frac{kC_0^2}{c-U_0}, \\ I=c-U_0+3\mathrm{i}kR^{-1}, \quad J=(\mathrm{i}kR)^{-1}. \end{gathered}\right\} \tag{A 21}$$

As before, all variables have been scaled with respect to the previously identified scale variables, the subscripts a and w refer to air and water respectively and $r=\rho_{\mathrm{a}}/\rho_{\mathrm{w}}$ and $m=\mu_{\mathrm{a}}/\mu_{\mathrm{w}}$.

The determinant of the matrix $[\boldsymbol{D}_{\mathrm{a}}-\boldsymbol{D}_{\mathrm{w}}]$ must be zero for the existence of non-trivial solutions of $\hat{\boldsymbol{\phi}}$. Expanding this determinant as the sums of the products of the second-order minors (a Laplace expansion) produces an expression for the determinant in terms of the components of the $\boldsymbol{y}(0)$ vector. The second-order minors are reduced and the determinant expanded to yield the eigenvalue relation:

$$[1_{\mathrm{a}}][6_{\mathrm{w}}]-[2_{\mathrm{a}}][5_{\mathrm{w}}]+[3_{\mathrm{a}}][4_{\mathrm{w}}]+[4_{\mathrm{a}}][3_{\mathrm{w}}]-[5_{\mathrm{a}}][2_{\mathrm{w}}]+[6_{\mathrm{a}}][1_{\mathrm{w}}]=0, \tag{A 22}$$

where

$$[1_{\mathrm{a}}]=y_{1\mathrm{a}}, \quad [1_{\mathrm{w}}]=y_{1\mathrm{w}}, \quad [2\mathrm{a}]=my_{2\mathrm{a}}, \quad [2_{\mathrm{w}}]=y_{2\mathrm{w}},$$

$$[3_a]=r[I_a y_{1a}+J_a y_{3a}], \quad [3_w]=I_w y_{1w}+J_w y_{3w},$$

$$[4_{\mathrm{a}}]=m[E_{\mathrm{a}} y_{2\mathrm{a}}-F_{\mathrm{a}} y_{1\mathrm{a}}+y_{4\mathrm{a}}], \quad [4\mathrm{w}]=E_{\mathrm{w}} y_{2\mathrm{w}}-F_{\mathrm{w}} y_{1\mathrm{w}}+y_{4\mathrm{w}}$$

$$[5_{\mathrm{a}}]=r[(E_{\mathrm{a}} I_{\mathrm{a}}-H_{\mathrm{a}}) y_{1\mathrm{a}}+E_{\mathrm{a}} J_{\mathrm{a}} y_{3\mathrm{a}}+J_{\mathrm{a}} y_{5\mathrm{a}},$$

$$[5_{\mathrm{w}}]=(E_{\mathrm{w}} I_{\mathrm{w}}-H_{\mathrm{w}}) y_{1\mathrm{w}}+E_{\mathrm{w}} J_{\mathrm{w}} y_{3\mathrm{w}}+J_{\mathrm{w}} y_{5\mathrm{w}},$$

$$[6_{\mathrm{a}}]=rm[F_{\mathrm{a}} I_{\mathrm{a}} y_{1\mathrm{a}}+F_{\mathrm{a}} J_{\mathrm{a}} y_{3\mathrm{a}}-H_{\mathrm{a}} y_{2\mathrm{a}}-I_{\mathrm{a}} y_{4\mathrm{a}}+J_{\mathrm{a}} y_{6\mathrm{a}},$$

$$[6_{\mathrm{w}}]=F_{\mathrm{w}} I_{\mathrm{w}} y_{1\mathrm{w}}+F_{\mathrm{w}} J_{\mathrm{w}} y_{3\mathrm{w}}-H_{\mathrm{w}} y_{2\mathrm{w}}-I_{\mathrm{w}} y_{4\mathrm{w}}+J_{\mathrm{w}} y_{6\mathrm{w}}.$$

A.4. *Calculation of the eigenfunctions*

Once the eigenvalue and the $\boldsymbol{y}$ terms have been obtained using the procedure described above, the complex eigenfunctions for air and water may be calculated. The form of the eigenfunction is assumed to be that of (A 5) with a separate eigenfunction system existing for each medium. Eliminating the constants in (A 5) will yield four equations composed of $\boldsymbol{y}$ terms and eigenfunction terms (Ng & Reid 1979) which are, in general form,

$$y_1\phi''-y_2\phi'+y_4\phi=0, \quad y_1\phi'''-y_3\phi'+y_5\phi=0, \tag{A 23, A 24}$$

$$y_2\phi'''-y_3\phi''+y_6\phi=0, \quad y_4\phi'''-y_5\phi''+y_6\phi'=0. \tag{A 25, A 26}$$

In principle, any of the four above equations may be integrated to determine the eigenfunction. Ng & Reid (1979) indicate that a backwards integration of (A 23) will do the best job of avoiding runaway numerical growth; we followed this direction and utilized a fourth-order Runge–Kutta scheme to obtain the eigenfunctions in air and water at a specific wavenumber, shown in figure 8.

REFERENCES

Chapman, D. R. & Kuhn, G. D. 1986 The limiting behavior of turbulence near a wall. *J. Fluid Mech.* **170**, 265–292.

Davey, A. 1979 On the removal of the singularities from the Ricatti method. *J. Comput. Phys.* **30**, 137–144.

DRAZIN, P. G. & REID, W. H. 1981 *Hydrodynamic Stability*, 1st edn. Cambridge University Press.

GASTEL, K. VAN, JANSSEN, P. A. E. M. & KOMEN, G. J. 1985 On phase velocity and growth rate of wind-induced gravity–capillary waves. *J. Fluid Mech.* **161**, 199–216.

GERALD, C. F. & WHEATLEY, P. O. 1985 *Applied Numerical Analysis*, 3rd edn. Addison-Wesley.

KAWAI, S. 1979 Generation of initial wavelets by instability of a coupled shear flow and their evolution to wind waves. *J. Fluid Mech.* **93**, 663–701.

LAKIN, W. D. & GROSCH, C. E. 1982 Higher modes of the Orr–Sommerfeld problem for boundary layer flows. *NASA Contract Rep.* NAGI-175.

LARSON, T. R. & WRIGHT, J. W. 1975 Wind-generated gravity–capillary waves: laboratory measurements of temporal growth using microwave backscatter. *J. Fluid Mech.* **70**, 417–436.

LOCK, R. C. 1954 Hydrodynamic stability of the flow in the laminar boundary layer between parallel streams. *Proc. Camb. Phil. Soc.* **50**, 105–124.

MILES, J. W. 1957*a* On the generation of surface waves by shear flows. Part 1. *J. Fluid Mech.* **3**, 185–204.

MILES, J. W. 1957*b* On the velocity profile for turbulent flow near a smooth wall. *J. Aero Sci.* **24**, 704.

NG, B. S. & REID, W. H. 1979 An initial value method for eigenvalue problems using compound matrices. *J. Comput. Phys.* **30**, 125–136.

SCHLICHTING, H. 1979 *Boundary Layer Theory*, 7th edn. McGraw-Hill.

TOBA, Y. & MITSUYASU, H. 1985 *The Ocean Surface: Wave Breaking, Turbulent Mixing and Radio Probing*. Reidel.

VALENZUELA, G. R. 1976 The growth of gravity-capillary waves in a coupled shear flow. *J. Fluid Mech.* **76**, 229–250.

WUEST, W. 1949 Beitrag zur Entstehung von Wasserwellen durch Wind. *Z. Angew. Math. Mech.* **29**, 239–252.